ADVANCED MATERIALS
www.advmat.de

Operando Tailoring of Defects and Strains in Corrugated β-Ni(OH)$_2$ Nanosheets for Stable and High-Rate Energy Storage

Shaofeng Li, Nikhil Sharma, Chang Yu, Yan Zhang, Gang Wan, Rong Fu, Hongling Huang, Xueyan Sun, Sang-Jun Lee, Jun-Sik Lee, Dennis Nordlund, Piero Pianetta, Kejie Zhao,* Yijin Liu,* and Jieshan Qiu**

Nickel hydroxide represents a technologically important material for energy storage, such as hybrid supercapacitors. It has two different crystallographic polymorphs, α- and β-Ni(OH)$_2$, showing advantages in either theoretical capacity or cycling/rate performance, manifesting a trade-off trend that needs to be optimized for practical applications. Here, the synergistic superiorities in both activity and stability of corrugated β-Ni(OH)$_2$ nanosheets are demonstrated through an electrochemical abuse approach. With ≈91% capacity retention after 10 000 cycles, the corrugated β-Ni(OH)$_2$ nanosheets can deliver a gravimetric capacity of 457 C g^{-1} at a high current density of 30 A g^{-1}, which is nearly two and four times that of the regular α- and β-Ni(OH)$_2$, respectively. Operando spectroscopy and finite element analysis reveal that greatly enhanced chemical activity and structural robustness can be attributed to the in situ tailored lattice defects and the strain-induced highly curved micromorphology. This work demonstrates a multi-scale defect-and-strain co-design strategy, which is helpful for rational design and tuned fabrication of next-generation electrode materials for stable and high-rate energy storage.

Efficient energy storage and conversion are highly demanded, and indispensable in our global energy outlook with a strong emphasis on the sustainability.[1–4] Hybrid supercapacitors (HSCs) are a class of energy storage devices with great potential due to their superior and balanced power and energy densities as well as long cycle life.[5,6] The root cause of these advantageous characteristics is associated with the HSCs' functioning mechanism, which features the synergy between the electrochemical reactions that occur on the surface (as in a capacitor) and in the bulk (as in a battery). Ni(OH)$_2$ is a well-known battery-type electrode for HSCs owing to its superior redox activity.[7,8] The two different crystallographic polymorphs, α- and β-Ni(OH)$_2$, show pros and cons in different performance attributes. In contrast to the β-Ni(OH)$_2$,which is characterized by closely-packed hexagonal Ni(OH)$_2$ layers, the α-Ni(OH)$_2$ consists of Ni(OH)$_2$ layers with intercalated anions or water.[8] By virtue of its high theoretical capacity (1035 C g^{-1}), the α-Ni(OH)$_2$ has been extensively investigated,[7,9,10] but its poor electrochemical stability and rate capability has limited its applications, which is largely attributed to the irreversible α-to-β phase transition in alkaline electrolyte.[9] Thus far, tremendous efforts have been devoted to tackle the challenge in promoting the stability of α-Ni(OH)$_2$. The reported approaches include nanostructuring,[11] composite with conductive material,[12–14] and doping with other transition metal cations (Al, Co, Mn, etc.).[7,9,15] Although incremental improvements in the electrochemical stability and rate capability have been demonstrated for α-Ni(OH)$_2$, the long-term cycling performance and rate capability at large current density are still far

Dr. S. Li, Prof. C. Yu, R. Fu, H. Huang, X. Sun, Prof. J. Qiu
State Key Lab of Fine Chemicals
School of Chemical Engineering
Liaoning Key Lab for Energy Materials and Chemical Engineering
Dalian University of Technology
Dalian 116024, P. R. China
E-mail: chang.yu@dlut.edu.cn; jqiu@dlut.edu.cn

N. Sharma, Prof. K. Zhao
School of Mechanical Engineering
Purdue University
West Lafayette, IN 47907, USA
E-mail: kjzhao@purdue.edu

The ORCID identification number(s) for the author(s) of this article can be found under https://doi.org/10.1002/adma.202006147.

DOI: 10.1002/adma.202006147

Y. Zhang, Dr. G. Wan, Dr. S.-J. Lee, Dr. J.-S. Lee, Dr. D. Nordlund, Prof. P. Pianetta, Dr. Y. Liu
Stanford Synchrotron Radiation Lightsource
SLAC National Accelerator Laboratory
Menlo Park, CA 94025, USA
E-mail: liuyijin@slac.stanford.edu

Y. Zhang
School of Materials Science and Engineering
Tianjin University
Tianjin 300072, P. R. China

Prof. J. Qiu
State Key Laboratory of Chemical Resource Engineering, College of Chemical Engineering
Beijing University of Chemical Technology
Beijing 100029, P. R. China
E-mail: qiujs@mail.buct.edu.cn

from satisfactory. Another relatively unexplored approach is to look into the β-$Ni(OH)_2$, which is regarded as a conventional material that suffers from its intrinsic low activity. To boost the activity of β-$Ni(OH)_2$ without jeopardizing the rate capability and electrochemical stability, material engineering efforts have to systematically tackle the local chemical environment at the atomic-scale,[16,17] the ion transportation properties at the nano/mesoscales,[18,19] and the chemomechanical robustness at the macroscale.[20,21] All in all, a simple, cost efficient, and multi effects material design approach needs to be explored, posing a frontier challenge in this field.

Here, we present a corrugated β-$Ni(OH)_2$ with deliberately tailored lattice vacancies and tensile strain as a highly active and stable HSCs electrode. Using NiV layered double hydroxide (NiV-LDH) as precursor, a facile self-sacrifice strategy involving an electrochemical abuse process, is developed to form corrugated β-$Ni(OH)_2$ nanosheets in situ. The corrugated β-$Ni(OH)_2$ exhibits a gravimetric capacity of 457 C g^{-1} at a current density of 30 A g^{-1}, which is ≈two and ≈four times that of the regular α-$Ni(OH)_2$ (214 C g^{-1}) and β-$Ni(OH)_2$ (118 C g^{-1}), respectively. Furthermore, it retained ≈91% of its initial capacity after 10 000 cycles at a current density of 6 A g^{-1} (a fivefold increment in lifetime comparing to the regular α-$Ni(OH)_2$). Using the cutting-edge operando X-ray absorption fine structure (XAFS) technique, the irreversible oxidation and dissolution of vanadium at high voltage was identified as the origin of the rapid α to β phase transformation and the formation of local lattice defects (5-coordinated Ni sites) and disordered areas, which result in the curved microstructure with tensile strain (2.3%). Finite element analysis was used to elucidate the fundamental mechanisms of the morphological reconstruction and the improvement in the mechanical robustness. This work highlights an in situ multi-scale tuning defect-and-strain strategy, which shows potential in the development of next-generation high-rate energy storage materials.

As shown in **Figure 1**a, the corrugated β-$Ni(OH)_2$ nanosheets with deliberately tailored strain and lattice vacancies were derived from NiV-LDH via an electrochemical abuse process. The original NiV-LDH was grown on the carbon fiber paper (CFP) using a hydrothermal method [details in the Supporting Information]. The scanning electron microscopy (SEM) images show that vertically oriented NiV-LDH nanosheets with a lateral size of ≈600 to 800 nm self-assemble on the CFP (Figure 1b and Figure S1a,b, Supporting Information). The high-resolution transmission electron microscopy (HR-TEM) image of NiV-LDH shows the visible lattice fringes with a spacing of ≈0.20 nm and 0.26 nm (Figure 1c) , which can be assigned to the (018) and (012) planes of LDH phase, respectively.[13] After the 5th cyclic voltammetry (CV) cycle over a voltage window of 0–0.7 V, the nanosheets (denoted as 0.7–5) show a slightly curved structure, accompanied by the formation of disorder phase and dislocations (Figure 1d,e). After the 9th CV cycling (0–0.7 V), the nanosheets (denoted as 0.7–9) develop a highly curved morphology with more disorder phase and dislocations (Figure 1f,g and Figure S1c,d, Supporting Information). The HR-TEM image (Figure 1g) shows that the small crystalline grains are surrounded by interspersed disordered domains, and the lattice spacing of 0.27 nm corresponds to the (100) planes of β-$Ni(OH)_2$.[22]

The energy-dispersive spectroscopy (EDS) result reveals that the atomic concentration of vanadium in NiV-LDH rapidly decreases from 22.2% to 1.6% after the 5th cycle, and then further drops to 0 after the 9th cycle (Figure S2, Supporting Information), indicating a complete dissolution of vanadium during the high-voltage CV cycling. It should be pointed out that although the morphology of the nanosheets evolved after the 5th and 9th cycles, the thickness of the nanosheets remains around 10 nm (Figure S3, Supporting Information), which indicates that the vanadium dissolution results in negligible effect on the thickness of the nanosheets. The X-ray diffraction (XRD) patterns further reveal a phase transformation from the α-$Ni(OH)_2$ to the β-$Ni(OH)_2$ that occurs during the CV cycling (Figure S4, Supporting Information). Specifically, no diffraction peaks of α-$Ni(OH)_2$ are detected after the 5th cycle, and all the new diffraction peaks can be clearly identified and indexed as the (001), (100), (101,) and (110) planes of the β-$Ni(OH)_2$, respectively. Such a phase transformation not only leads to a dramatic decrease in interlayer spacing along *c*-axis (from 7.8 to 4.6 Å), but also results in a 1.3% tensile strain along *a* and *b*-axis due to the expansion of the lattice parameter from 3.08 to 3.12 Å (Figure 1a).

To further reveal the local coordination environment of Ni cations during the CV cycling, operando XAFS over the Ni K-edge was performed based on our previously established method.[23] The Fourier transform (FT) of the extended XAFS (FT-EXAFS) spectra reveal that the intensity of the two peaks at 1.59 and 2.75 Å gradually reduces upon cycling (Figure 1h), indicating that more Ni cations transform into a state with unsaturated coordination.[24,25] The positive shift of Ni—Ni/V peaks further implies an increment in the Ni—Ni/V bond length upon CV cycling. As shown in Figure 1i and the EXAFS fitting results (Figure S5 and Table S1, Supporting Information), after the 5th and the 9th cycles, the Ni—O coordination number (N(Ni—O)) is decreased from 6.0 to 5.4, and then to 5.0, suggesting the increment of the oxygen vacancies in the corrugated β-$Ni(OH)_2$ with distorted Ni octahedron structure. Similarly, the Ni—Ni/V coordination number (N(Ni—Ni/V)) is also decreased from 6.0 to 5.1, and then to 4.5, further indicating the increase of the vanadium vacancies around Ni cations, echoing the observed vanadium dissolution during the CV cycling. In addition, the Ni—Ni/V bond length is increased from 3.08 to 3.12, and then to 3.15 Å after the 5th and the 9th cycles, indicative of an increased tensile strain of 1.3% and 2.3% along the *a*- and *b*-axis. As summarized in Figure 1i, the formation of the corrugated β-$Ni(OH)_2$ nanosheets can be divided into two processes as illustrated in the schematic in Figure 1a. At the first stage (the first 5 cycles), the vanadium dissolution results in the nucleation of the disorder domains and the phase transformation (α to β), which initiates the formation of the curved microstructure. The dissolution of vanadium is closely associated with the formation of the lattice vacancies. And the α to β phase transformation not only leads to a dramatically decreased interlayer spacing (from 7.8 to 4.6 Å) along the *c*-axis, but also causes an in-plane tensile strain of 1.3%. After this initiation process, the subsequent vanadium dissolution in the following CV cycles intensifies the local disordering and structural reconstruction, and further leads to the highly curved β-$Ni(OH)_2$ nanosheets with an increased tensile strain of 2.3%.

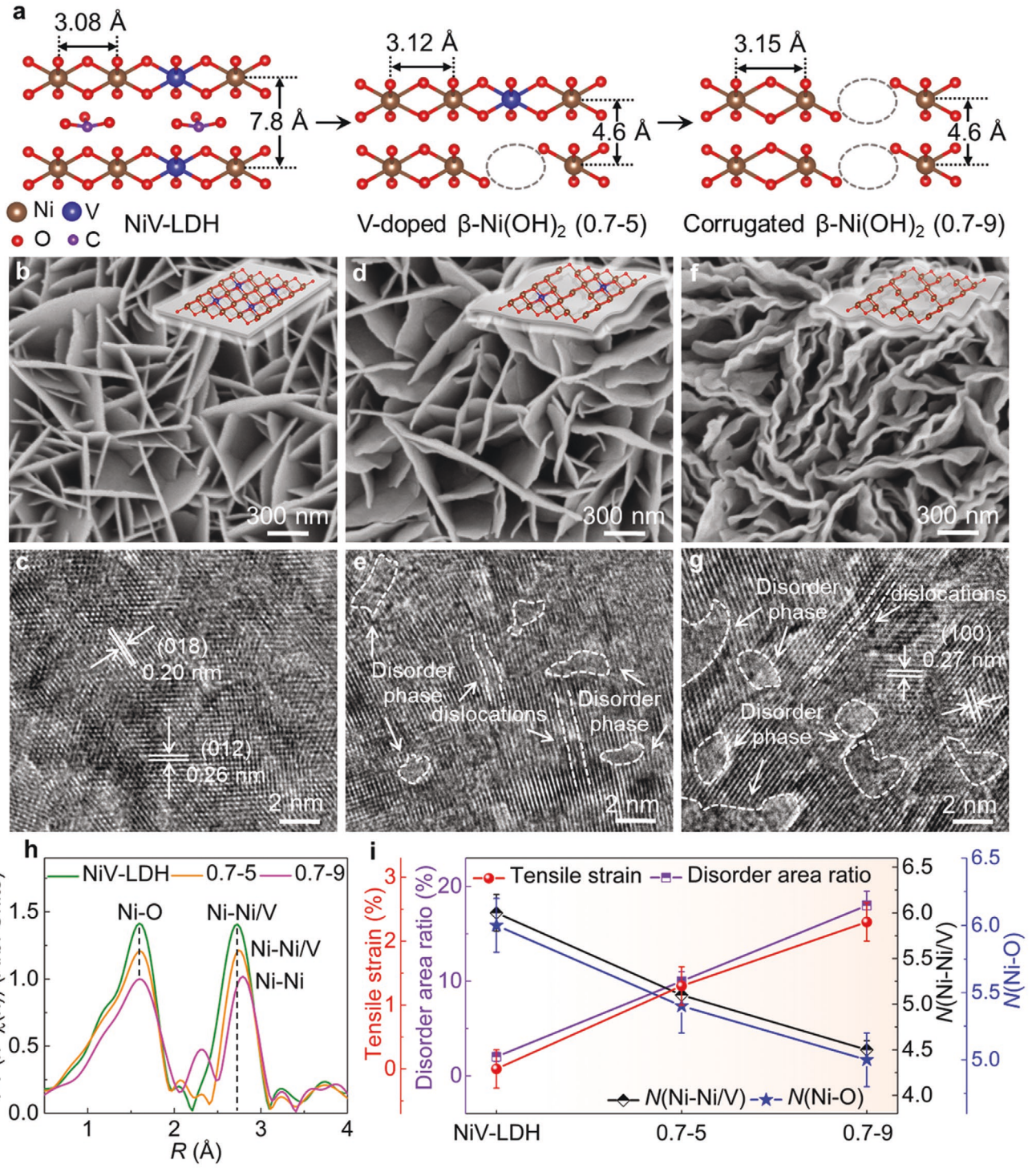

Figure 1. Fabrication process and structural characterization of corrugated β-Ni(OH)$_2$. a) Schematic showing the formation of corrugated β-Ni(OH)$_2$ nanosheets from the stiff NiV-LDH nanosheets with the dissolution of vanadium and increasing tensile strain. b) SEM and c) HR-TEM images of the NiV-LDH. d) SEM and e) HR-TEM images of the NiV-LDH after the 5th cycling. f) SEM and g) HR-TEM images of the NiV-LDH after the 9th cycling. h) Operando FT-EXAFS spectra at Ni K-edge for the NiV-LDH under different stages. i) Tensile strain, disorder area, Ni—Ni/V and Ni—O coordination number of the NiV-LDH under different stages.

To unveil the origin of the structural evolution during the high voltage CV cycling, we carried out operando XAFS measurements over both V and Ni K-edges. The CV curves of the first 14 cycles over 0–0.7 V are shown in the Figure S6, Supporting Information, suggesting that the CV curves are tending to stabilize after the 9th cycle. As shown in **Figure 2**a,b, the

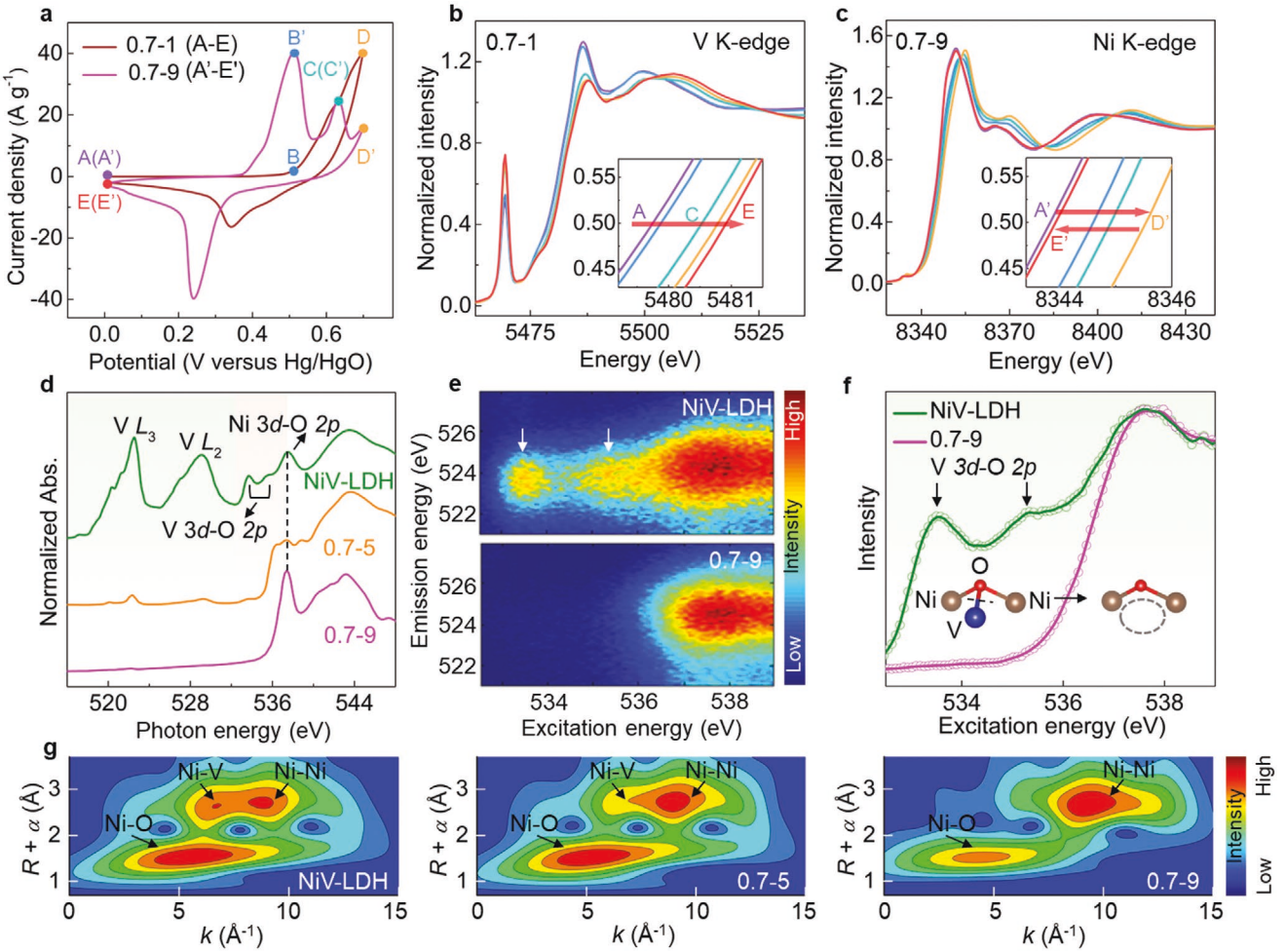

Figure 2. Operando XANES measurement and surface electronic structure of the NiV-LDH under different stages. a) Operando CV curves of the 1st and 9th cycles for the NiV-LDH electrode within 0–0.7 V at a scan rate of 5 mV s^{-1}. b,c) Operando XANES spectra recorded at the V K-edge during the 1st cycle (b) and Ni K-edge during the 9th cycle (c) of the NiV-LDH electrode. d) V *L*-edge, O K-edge spectra of NiV-LDH under different stages. e) Oxygen RIXS maps and f) corresponding PFY spectra of NiV-LDH and after 9th cycles. g) WT-EXAFS maps of the NiV-LDH under different stages.

operando X-ray absorption near-edge structure (XANES) spectra recorded over the V K-edge was measured at five selected voltages (A:0 V, B: 0.5 V, C: 0.63 V, D: 0.7 V, E: 0 V) during the 1st CV cycle. It is clearly seen that the V K-edge XANES spectrum shifts toward high energy (Figure 2b), which implies the monotonic oxidation of V during the 1st cycle. For comparison, we conduct operando V K-edge XANES measurements on the electrode that is cycled over a regular voltage window of 0–0.55 V (Figure S7a, Supporting Information). We observe that, even after the 9th cycle over 0–0.55 V, the oxidation state of V is still lower than that of the electrode cycled over 0–0.7 V for only once. The comparison of the vanadium concentration after the CV cycling over different voltage windows also indicates that the amount of vanadium dissolution during the CV cycling over 0–0.55 V is much lower than that of 0–0.7 V (Figure S7b, Supporting Information). Therefore, the high-voltage cycling triggers the formation of high valence VO_x, which is more soluble and, therefore, is the origin of the vanadium dissolution upon CV cycling.[26] The electrochemical reaction mechanism could be explained by the following equation. During the high-voltage window range (>0.55 V), the NiV-LDH reacts with the OH^- rapidly, which not only results in the vanadium oxidation and the consequent dissolution, but also leads to the formation of corrugated β-$Ni(OH)_2$.

$$4Ni_{0.75}V_{0.25}\left(CO_3^{2-}\right)_{0.125}\left(OH^-\right)_2 \bullet H_2O + 2OH^- \rightarrow 3Ni(OH)_2 + VO_2 + 6H_2O + 0.5CO_3^{2-} + e^- \quad (1)$$

In addition, even after the 9th cycle over 0–0.55 V, the electrode still exhibits the same flat morphology without obvious curvatures (Figure S7c,d, Supporting Information). It further indicates that a complete vanadium dissolution is essential to the formation of highly curved morphology. The XANES spectra over the Ni K-edge was also recorded at the same selected voltages (A' to E') during the 9th CV cycle (Figure 2c). The Ni redox reaction upon CV cycling demonstrates good reversibility. Compared with these bulk-averaged techniques, for example, XAFS and XRD, the soft X-ray absorption spectroscopy (sXAS) could identify the oxidation states and chemical bond with surface sensitivity, and could offer more detailed information on

the local electronic structure.[27] Specifically, the intensity portion of the multiplet structures in sXAS spectra can be used as a descriptor to distinguish the relative oxidation states of the transition metals cations.[28] As shown in the V *L*-edge and O K-edge spectra (measured in total electron yield (TEY) mode with probing depth at ≈5 nm, Figure 2d), the intensity of both V L_3-edge and L_2-edge decreases after the 5th cycle and completely disappears after the 9th cycle. This can be ascribed to the vanadium dissolution in the electrode. In addition, both the absorption peaks around 533.7 and 536.0 eV, which are assigned to the hybrid state of O *2p* to V *3d*, also exhibit a similar trend as the V *L*-edge data. It should be noted that the increased intensity of the absorption peaks around 536.0 eV after 5th cycle could be attributed to the incomplete dissolution and the consequent vanadium residual on the surface.

In contrast, the peak at around 537.4 eV, which is attributed to the hybrid state of O *2p* to Ni *3d*, remains unchanged. The Ni *L*-edge spectra also reveal the negligible change in the valence state of Ni cations after the high-voltage CV cycling (Figure S8, Supporting Information). Considering the close relationship between oxygen chemical environment and activity of the transition metal compounds for battery-type electrode, the resonant inelastic X-ray scattering (RIXS) with a probing depth of ≈150 nm (i.e., bulk sensitive for the nanosheets) was further employed to reveal the oxygen coordination structure.[27,29,30] In addition, the transition edge sensor (TES) detectors were used for the RIXS measurements. The TES detectors are microcalorimeters with intrinsic energy resolution, which could improve the detection sensitivity by eliminating the fluorescence background in soft X-ray range. In particular, the partial fluorescence yields (PFY) signal extracted from the RIXS data rejects unwanted photons, and further enhances the signal-to-noise ratio of the spectra. As shown in the O K-edge RIXS maps (Figure 2e), the two features centered at excitation energy of 533.7 and 536.0 eV (assigned to the O *2p* to V *3d* hybrid state) exist in the pristine NiV-LDH. After the 9th cycle, these two features are completely suppressed in the RIXS map and the corresponding PFY spectra (Figure 2f). This data suggests the bond breaking of V—O in the bulk of the electrode, not just on the surface. The similar phenomenon can also be observed in the wavelet transform (WT) analyses for the k^2-weighted EXAFS (WT-EXAFS) over Ni K-edge. The WT analysis is a powerful method to distinguish the overlapping contributions in radial distance that come from neighboring atom with multiple-scattering.[31,32] By combining the radial distance resolution and *k*-space resolution, WT-EXAFS separates backscattering atoms in the *k*-space. As shown in Figure 2g, the gradually disappearing intensity maximum at ≈7 $Å^{-1}$ (assigned to the Ni—V coordination) also indicates the Ni—V bond breaking in the bulk of the electrode. Therefore, based on these results, the vanadium cations are more susceptible to be oxidized to high valence state during the high-voltage CV cycling, accompanied by the V—O and Ni—V bond breaking, which further results in the complete vanadium dissolution from the electrode. It not only forms the disordered areas, but also leads to oxygen and vanadium vacancies and, ultimately results in the highly curved β-$Ni(OH)_2$ nanosheets with increased tensile strain.

The specific activity of the NiV-LDH electrode, as well as that of the NiV-LDH after the 5th and the 9th cycles over 0–0.7 V were tested using a three-electrode setup with 6 M KOH aqueous solution as electrolyte. It should be noted that the stable voltage window of 0–0.55 V was selected for the electrochemical performance evaluation for a fair comparison with the literature reports. As shown in Figure S9a, Supporting Information, all the CV curves exhibit similiar shape with a pair of intense redox peaks that are related to the $Ni(OH)_2$/NiOOH. Moreover, the redox peak intensity is enhanced in the 0.7–5 and 0.7–9 electrodes, implying the elevated specific capacity. The galvanostatic charge/discharge (GCD) curve was further used to calculate the specific capacity of these electrodes (Figure S9d–f, Supporting Information). As shown in **Figure 3**a, the 0.7–9 electrode exhibits an outstanding gravimetric capacity of 746 C g^{-1} at a current density of 1 A g^{-1}, which is higher than that of the 0.7-5 electrode (488 C g^{-1}) and the NiV-LDH (347 C g^{-1}). Such a greatly improved specific activity of the 0.7–5 and the 0.7–9 electrodes can be attributed to the enhanced tensile strain and the increased oxygen and vanadium vacancies.

For comparing the specific activity of the corrugated β-$Ni(OH)_2$ (i.e., the 0.7–9 electrode) versus the regular β-$Ni(OH)_2$ and α-$Ni(OH)_2$, monocrystalline β-$Ni(OH)_2$ and polycrystalline α-$Ni(OH)_2$ nanosheets were also prepared based on previous literature.[33,34] It should be noted that all of these materials were vertically grown onto the CFP and used as the working electrode (mass loading of corrugated β-$Ni(OH)_2$: 3.34 mg cm^{-2}, regular β-$Ni(OH)_2$: 2.04 mg cm^{-2}, regular α-$Ni(OH)_2$: 2.02 mg cm^{-2}). As shown in Figure S10, Supporting Information, the morphology of both the regular β-$Ni(OH)_2$ and α-$Ni(OH)_2$ are flat nanosheets without any obvious morphological curvatures. The HR-TEM image and fast Fourier transform (FFT) patterns further confirm the monocrystalline and polycrystalline structure of regular β-$Ni(OH)_2$ and α-$Ni(OH)_2$, respectively. XRD patterns further show that both regular and corrugated β-$Ni(OH)_2$ nanosheets have the same β-$Ni(OH)_2$ phase [JCPDS Card no. 14-0017]. While the regular β-$Ni(OH)_2$ is highly crystalline, the corrugated β-$Ni(OH)_2$ shows reduced crystallinity (Figure S11, Supporting Information). The diffraction peaks of (100) plane in corrugated β-$Ni(OH)_2$ are shifted toward the lower angle in comparison with that of the regular β-$Ni(OH)_2$, indicating a larger lattice constant (e. g. enhanced tensile strain) in the corrugated β-$Ni(OH)_2$ nanosheets. The EXAFS curve-fitting analysis further reveals the saturated coordination environment of Ni sites in both regular β-$Ni(OH)_2$ and α-$Ni(OH)_2$ (Figure S12 and Table S2, Supporting Information), which contrasts the vacancy-enriched lattice structure of the corrugated β-$Ni(OH)_2$.

As shown in Figure 3a,b and Figure S9b,c (Supporting Information), at a current density of 1 A g^{-1}, the gravimetric capacity of the corrugated β-$Ni(OH)_2$ (746 C g^{-1}) is considerably higher than that of the regular α-$Ni(OH)_2$ (636 C g^{-1}) and the regular β-$Ni(OH)_2$ (223 C g^{-1}, improved by a factor of 3.3). More importantly, the corrugated β-$Ni(OH)_2$ exhibits significantly improved rate capability. Specifically, the corrugated β-$Ni(OH)_2$ delivers a gravimetric capacity of 457 C g^{-1} at a current density of 30 A g^{-1}, with a high capacity retention of 61%, showing considerable advantages over regular α-$Ni(OH)_2$ (214 C g^{-1}, 34%) and regular β-$Ni(OH)_2$ (119 C g^{-1}, 53%). To the best of our knowledge, the herein reported high retention rate in corrugated β-$Ni(OH)_2$ is superior to most of the other kinds of β-$Ni(OH)_2$

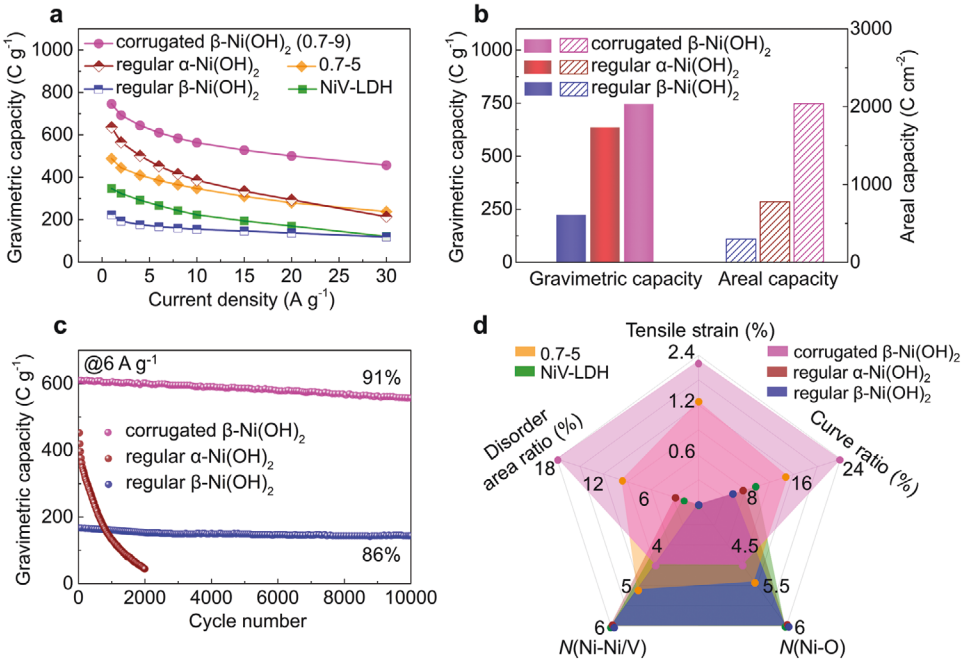

Figure 3. Electrochemical performance of the NiV-LDH, corrugated β-$Ni(OH)_2$, regular α-$Ni(OH)_2$, and β-$Ni(OH)_2$. a) Gravimetric capacity of the NiV-LDH under different stages at a range of current density from 1 to 30 A g^{-1}. b) Gravimetric and areal capacity of the corrugated β-$Ni(OH)_2$, regular α-$Ni(OH)_2$ and β-$Ni(OH)_2$ at the current density of 1 A g^{-1} and 20 mA cm^{-2}, respectively. c) Long-term cycling performance of the corrugated β-$Ni(OH)_2$, regular α-$Ni(OH)_2$ and β-$Ni(OH)_2$ at the current density of 6 A g^{-1}. d) The comparison of the tensile stain, Ni—Ni/V and Ni—O coordination number, disorder area, and curve ratio for different electrodes.

under comparable conditions (see comparison with various nanostructuring synthesize efforts in Table S3, Supporting Information).

Moreover, benefiting from the high mass loading of active materials in our electrode configuration, the corrugated β-$Ni(OH)_2$ shows even more significant advantages under high areal current density. The corrugated β-$Ni(OH)_2$ achieves an areal capacity of 2039 C cm^{-2} at current density of 20 mA cm^{-2} (Figure 3b), which is ≈2.6 times that of regular α-$Ni(OH)_2$ (779 C cm^{-2}) and ≈6.8 times that of regular β-$Ni(OH)_2$ (299 C cm^{-2}). Even under a current density of 100 mA cm^{-2}, the corrugated β-$Ni(OH)_2$ delivers an areal capacity of 1526 C cm^{-2} (Figure S13, Supporting Information). We highlight here that the corrugated β-$Ni(OH)_2$ maintains 91% of the initial capacity after 10 000 cycles at a current density of 6 A g^{-1} (Figure 3c), which is superior to regular β-$Ni(OH)_2$ and five times longer in lifetime compared with regular α-$Ni(OH)_2$. The CV curve of the corrugated β-$Ni(OH)_2$ electrode after 10 000 cycles also shows similar shape as that of after the 1st cycle without noticeable difference in integrated area (Figure S14, Supporting Information), indicative of the superior electrochemical stability.

The reduced semicircle diameter shown in electrochemical impedance spectroscopy (EIS) further reveals the improved transport properties of the charge carriers in the corrugated β-$Ni(OH)_2$ (Figure S15, Supporting Information). Such enhanced interfacial charge transport properties may result from the abundant defects in the corrugated β-$Ni(OH)_2$ nanosheets. The kinetic process of the corrugated β-$Ni(OH)_2$ was also evaluated at varied scan rates (0.5 to 2 mV s^{-1}, Figure S16a, Supporting Information). As shown in Figure S16b (Supporting Information), both anodic and cathodic peak current slopes of the corrugated β-$Ni(OH)_2$ electrode are close to 0.5, indicating that the kinetics in corrugated β-$Ni(OH)_2$ electrode are dominated by the diffusion-controlled reactions. In addition, the corrugated β-$Ni(OH)_2$ electrode achieves capacitive contribution no more than 20% in a range of 0.5 to 2 mV s^{-1} (Figure S16c, Supporting Information), which further confirms that the corrugated β-$Ni(OH)_2$ is battery-type material.

Based on these results, the outstanding electrochemical performance of the corrugated β-$Ni(OH)_2$ nanosheets can be ascribed to the unique local lattice geometry and the micromorphology (Figure 3d): (1) the highly curved nanosheets with plentiful disorder area provide abundant electroactive sites for highly efficient utilization of β-$Ni(OH)_2$; (2) the unsaturated 5-coordinated Ni sites with oxygen and vanadium vacancies exhibit more optimal redox reaction energy barrier, which is beneficial to the redox activity and the reversible charge storage properties; (3) the enhanced tensile strain in the corrugated nanosheets provide appropriate cushion to reduce the strain during repeated redox reactions and, subsequently, prolong the life-span of the electrode that is operated under large current density. In addition, the corrugated β-$Ni(OH)_2$ delivers much better rate capability and cycling performance than regular α-$Ni(OH)_2$, and much higher capacity than regular β-$Ni(OH)_2$. Compared with corrugated β-$Ni(OH)_2$, both regular α-$Ni(OH)_2$ and β-$Ni(OH)_2$ show flat morphology with saturated coordination environment of Ni sites. Therefore, the highly curved nanosheets with plentiful oxygen and vanadium vacancies, as well as the enhanced tensile strain are essential to the remarkable electrochemical performance of the corrugated β-$Ni(OH)_2$.

To further elucidate the formation mechanism of the corrugated β-Ni(OH)$_2$ nanosheets and the enhanced mechanical reliability upon electrochemical cycling, the finite element analysis (FEA) was performed. We simulate the formation of the corrugated morphology when the pristine NiV-LDH is subject to the mechanical strain induced by the phase transformation. Details are described in the Experimental Section. The phase change from the α-Ni(OH)$_2$ to the β-Ni(OH)$_2$ results in an increase in the lattice parameters along the *a*- and *b*-axis and a decrease in the lattice parameter in the *c*-axis. Therefore, at the atomic level, the crystal structure exhibits a tensile strain in the *a*- and *b*-axis and a compressive strain in the *c*-axis. These anisotropic strains are originated at the atomic-level. They accumulate and propagate until they meet the boundary conditions as the nanosheets are fixed on the CFP and the deformation along the *a*-, *b*-, and *c*-axis directions are physically constrained. Such a constrained deformation, in turn, converts the atomic-level lattice strains into macroscopic-level mechanical forces, which are compressive in the *a*-axis direction and tensile in the *c*-axis direction (**Figure 4**b). In addition to the mechanical force, the presence

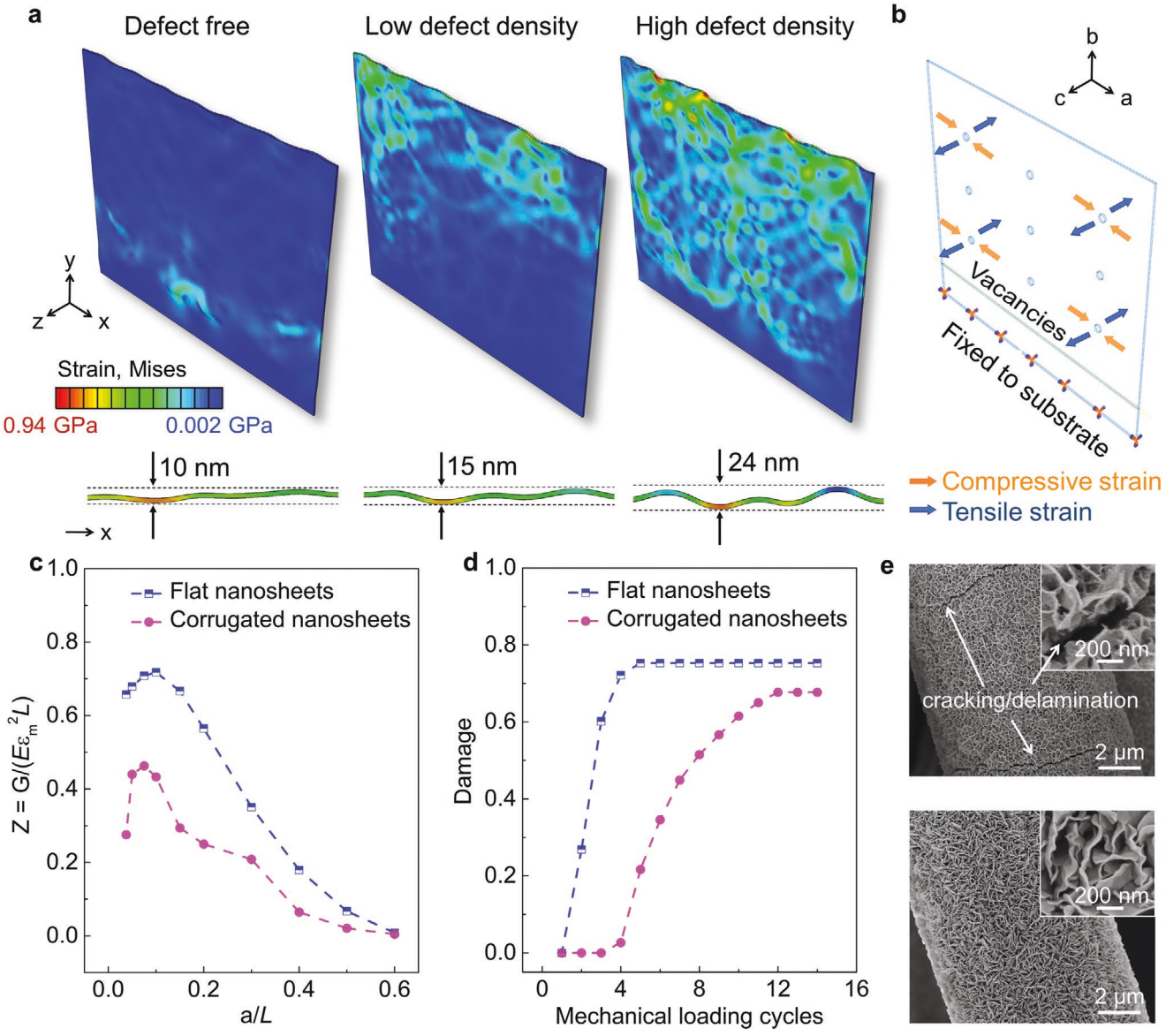

Figure 4. Theoretical results of the formation mechanism and mechanical stability of corrugated β-Ni(OH)$_2$ nanosheets. a) Plots of von Mises strain and *c*-axis displacement in nanosheets depicting corrugation formation process for 0%, 8%, and 18% disordered regions. With an increase in fraction of disordered region, more prominent corrugation is observed for same loading and boundary conditions on nanosheet. b) Schematic of strain direction on nanosheet during phase change from α-Ni(OH)$_2$ to β-Ni(OH)$_2$ with bottom part constrained to carbon fiber substrate. c) Plot of dimensionless energy release rate as a function of crack length in flat and corrugated nanosheet. d) Damage function for cohesive elements between nanosheet and substrate as a function of charge–discharge cycles. Damage = 1 represents failure of all cohesive elements and complete detachment of nanosheet from the substrate. e) SEM images of the regular β-Ni(OH)$_2$ (top panel) and corrugated β-Ni(OH)$_2$ nanosheets (bottom panel) after 10 000 cycles, confirming robustness of corrugated structure.

of the disordered regions in the nanosheets (Figure 1c,e,g) is another major cause for the formation of the corrugated morphology. These disordered regions are induced by the high-voltage cycling and are dispersed throughout the nanosheets. They could effectively deform the morphology of nanosheets in response to the lattice strains from the neighboring crystalline domains.

To elucidate the effect of the disordered regions in the formation process, we simulate three cases with different amounts (0%, 8%, and 18%, Figure 4a), of disordered phase based on the ratio of disorder area shown in Figure 1c,e,g. When the fraction of the disordered area increases, the amplitude of corrugation enlarges. The different fractions and distributions of the disordered phase can significantly alter the corrugated morphology. The three cases modeled here do not exclude other possible configurations but illustrate that the macroscopic-level compressive mechanical force and the disordered phase within the nanosheets altogether generate the corrugated pattern. We further demonstrate that the highly curved morphology is beneficial to the electrochemical stability of the corrugated $Ni(OH)_2$. As shown in Figure 1, the pristine NiV-LDH transforms into the highly curved β-$Ni(OH)_2$ after 9 cycles. In the following cycles, the nanosheets reversibly transform into NiOOH (a = 2.81 Å, b = 2.81 Å, c = 4.84 Å) during the charging process and revert back to β-$Ni(OH)_2$ (a = 3.126 Å, b = 3.126 Å, c = 4.605 Å) during the discharging process. The cyclic charging and discharging induce repetitive changes in the lattice constants, which would reduce the mechanical integrity of the structure.

Here, we demonstrate the enhanced mechanical reliability of the electrochemically abused β-$Ni(OH)_2$ by comparing the driving force of crack in the flat and corrugated nanosheets. The theory is outlined in the Experimental Section. Figure 4c plots the energy release rate (dimensionless quantity $Z = G/(E\varepsilon_m{}^2L)$) for the flat and corrugated configurations when the size of the pre-existing crack (a/L) varies.[35] When the crack is very short, the elastic energy in the nanosheets does not change appreciably as the crack grows, and the energy release rate is small. Likewise, when the crack is very long, the elastic energy is nearly fully relaxed because the crack introduces larger constraint-free area, and the energy release rate is also small. In between the two limits, the energy release rate reaches the maximum value for a crack of a certain length. This overall behavior holds for both the flat and corrugated structures, but the curved nanosheets exhibit a much smaller value of the energy release rate at any given crack length, indicating a greatly improved resistance to crack growth.

We further model the dynamics of crack growth at the interface between the nanosheet and the substrate during the electrochemical cycling using a cohesive zone model. Figure 4d shows the evolution of the damage function in the flat and corrugated nanosheets in different mechanical loading cycles. The definition of the damage function is described in the Experimental Section. It should be noted that the goal of this modeling is not to replicate the long-term cycling of β-$Ni(OH)_2$ in experiments, but to demonstrate the improved mechanical stability in electrochemically abused nanosheets. The comparison in Figure 4d shows the larger resistance of corrugated nanosheet for damage initiation in the first few loading cycles and resilience against damage growth in later loading cycles relative to the flat geometry. Therefore, the qualitative comparison clearly demonstrates that the robust mechanical reliability of corrugated nanosheets maintains the interfacial integrity of the system and contributes to the stable electrochemical performance over long-term cycling. This theoretical understanding corroborates the experimental observation of much less cracks in the long-term cycled nanosheets as shown in Figure 4e.

In summary, high-efficiency and stable β-$Ni(OH)_2$ was developed by a multi-scale tuning strain-and-defect strategy via the controlled vanadium dissolution. Operando XAFS has revealed that vanadium is more susceptible to the high voltage electrochemical environment, and undergoes an irreversible and monotonic oxidation and sequent self-sacrificial dissolution process. The subsequent α to β phase transformation and the development of disorder local regions facilitates the formation of the corrugated β-$Ni(OH)_2$ with controlled tensile stain and unsaturated Ni sites. The corrugated β-$Ni(OH)_2$ has shown an outstanding activity and stability for high-rate energy storage. The present work not only formulates a comprehensive understanding of the structure and morphology reconstruction in 2D nanosheets for HSCs applications, but also may inspire new pathways toward rational engineering of efficient and robust electrodes for stable and high-rate energy storage.

Experimental Section

Fabrication of Corrugated β-Ni(OH)$_2$: The corrugated β-$Ni(OH)_2$ was obtained after 9th CV cycling within voltage window of 0–0.7 V. The CV measurement was conducted on a standard electrochemical workstation (Bio-Logic SP-200) with a conventional three-electrode set up, using Hg/HgO electrode as reference electrode and Pt foil as counter electrode. The as-obtained NiV-LDH on CFP substrate was served as the working electrode directly.

Operando XAFS Measurements: Operando XANES and EXAFS are both measured at beamline 4–1 at the Stanford Synchrotron Radiation Lightsource (SSRL) with a standard electrochemical workstation (Bio-Logic SP-200). The standard V_2O_3, VO_2, and V_2O_5 were measured at the Shanghai Synchrotron Radiation Facility (SSRF, BL14W1). The Ni or V foils were used to calibrate all the XAFS spectra. The EXAFS data was processed using ATHENA module implemented in the IFEFFIT software package.[36] The ARTEMIS module of IFEFFIT were applied to do EXAFS curve-fitting analysis.

Soft XAS Measurements: sXAS spectra were measured at beamline 10–1 at SSRL. The free-standing electrodes were mounted on the conductive carbon tape, and then loaded on a sample holder in an ultra-high vacuum chamber for the measurement. The vertically polarized X-ray (sigma-polarization) was used, and the incident beam was monochromatized by a 600 lines mm^{-1} spherical grating monochromator, and its angle was set at 30 degrees from the sample surface. All the sXAS spectra were normalized by the intensity of the incoming X-ray beam that was concurrently measured as a drain current on an electrically isolated gold-coated mesh. A linear background, which was determined by the intensity of the pre-edge region, was subtracted from the data. RIXS measurement was performed at beamline 10–1 at SSRL using a TES spectrometer.[27,37] The TES spectrometer consists of a 240-channel energy-dispersive detector array facing the sample-X-ray interaction point at 90° with regard to the incoming X-ray beam. The distance between the interaction point and the TES detector array was 5 cm. To achieve higher energy resolution of the TES than in a normal operation mode, only a subset of the detector array (64 pixels) was employed during the O K-edge RIXS measurements. The energy measured by the TES was calibrated through separate measurements of a reference sample consisting of C, N, O, and various 3d transition-metal oxides with known emission energies.

Finite-Element Analysis: The computational modeling is performed using the commercial software ABAQUS/Explicit (SIMULIA, Providence, RI). A model of the size of 800 nm (length) × 600 nm (height) × 10 nm (thickness) as consistent with the experimental measurement of the β-$Ni(OH)_2$ nanosheets (Figure S1, Supporting Information) was constructed. The nanosheets were considered as being an elastic material with Young's modulus of 96 GPa and Poisson's ratio of 0.22[38] and the substrate CFP of the Young's modulus of 230 GPa and Poisson's ratio of 0.26. A sinusoidal perturbation with an amplitude of 1% of the nanosheet thickness was prescribed to induce buckling of the nanosheets upon compression in the *a*-axis.

The Griffith fracture mechanics were used and a pre-existing crack of various lengths at the interface of the nanosheet and the CFP substrate, was assumed. A sinusoidal function is used to construct the corrugated shape such that both the corrugated and flat sheets have same volume and are subject to similar boundary conditions. The *J*-integral was used to calculate the energy release rate *G*,[39] the driving force for the pre-existing crack to grow, in both configurations. Dimensional analysis dictates that the energy release rate *G* should take the form $G = ZE\varepsilon_m^2 L$, where *E* is Young's modulus of the nanosheet, *L* is a characteristic size which is taken as the length along the *a*-axis of the nanosheet, and ε_m is a characteristic mismatch strain, defined as $\varepsilon_m = (l_1 - l_0)/l_0$, where l_0 and l_1 are the lattice parameters in the initial state β-$Ni(OH)_2$ and at the charged state NiOOH, respectively. The a/L represents the size of pre-existing crack, where *a* and *L* is the length of crack and nanosheet along *a*-axis, respectively. At a given time, the distribution of the strain in the nanosheets is determined by solving the boundary value problems. The dimensionless coefficient *Z* is dependent on the geometry of the nanosheets, the location of the crack, and the length of the crack. It is also worth pointing out that the choice of the material parameters, the cohesive zone model, and the presence of disordered phases will likely alter the numerical values of $G = ZE\varepsilon_m^2 L$ and the damage function reported here.

In the cohesive zone modeling, cohesive elements are defined at the interface between the nanosheet and the substrate. A bi-linear cohesive traction-separation law is used to describe the constitutive behavior. The cohesive zone model has a fracture energy of 1 J m^{-2} and a tensile strength of 1 GPa. Once the strain energy surpasses the fracture energy, the cohesive elements separate from the substrate. A damage function for the cohesive elements was defined such that damage remained zero within the elastic deformation, started growth when the strain reached the tensile strength, and was equal to 1 when the strain energy exceeded the fracture energy.

Supporting Information

Supporting Information is available from the Wiley Online Library or from the author.

Acknowledgements

S.L. and N.S. contributed equally to this work. This work was partly supported by the National Natural Science Foundation of China (NSFC, No. 51872035), the Fundamental Research Funds for the Central Universities (DUT19LAB20), and the National Key Research Development Program of China (2016YFB0101201). Use of the SSRL, SLAC National Accelerator Laboratory, is supported by the U.S. Department of Energy (DOE), Office of Science, Office of Basic Energy Sciences under Contract No. DE-AC02-76SF00515. K.Z. is grateful for the support of the National Science Foundation through the grants CMMI-1726392 and DMR-1832707. This work also benefited from beamline BL14W1 station in Shanghai Synchrotron Radiation Facility (SSRF). S.L. appreciates the great support from the Chinese Scholarship Council (No. 201806060018). The authors acknowledge the experiment support from R. Davis and engineering support from D. Van Campen and V. Borzenets for the operando hard XAS experiment at SSRL.

Conflict of Interest

The authors declare no conflict of interest.

Keywords

defects, strain, supercapacitors, β-$Ni(OH)_2$

Received: September 9, 2020
Revised: October 19, 2020
Published online:

[1] X. Yang, C. Cheng, Y. Wang, L. Qiu, D. Li, *Science* **2013**, *341*, 534.
[2] P. Simon, Y. Gogotsi, B. Dunn, *Science* **2014**, *343*, 1210.
[3] M. Salanne, B. Rotenberg, K. Naoi, K. Kaneko, P. L. Taberna, C. P. Grey, B. Dunn, P. Simon, *Nat. Energy* **2016**, *1*, 16070.
[4] M. R. Lukatskaya, S. Kota, Z. Lin, M.-Q. Zhao, N. Shpigel, M. D. Levi, J. Halim, P.-L. Taberna, M. W. Barsoum, P. Simon, Y. Gogotsi, *Nat. Energy* **2017**, *2*, 17105.
[5] W. Zuo, R. Li, C. Zhou, Y. Li, J. Xia, J. Liu, *Adv. Sci.* **2017**, *4*, 1600539.
[6] S. Li, C. Yu, J. Yang, C. Zhao, M. Zhang, H. Huang, Z. Liu, W. Guo, J. Qiu, *Energy Environ. Sci.* **2017**, *10*, 1958.
[7] J. H. Lee, H. J. Lee, S. Y. Lim, K. H. Chae, S. H. Park, K. Y. Chung, E. Deniz, J. W. Choi, *Adv. Funct. Mater.* **2017**, *27*, 1605225.
[8] F. Dionigi, P. Strasser, *Adv. Energy Mater.* **2016**, *6*, 1600621.
[9] P. V. Kamath, *J. Electrochem. Soc.* **1994**, *141*, 2956.
[10] Y. Chen, W. K. Pang, H. Bai, T. Zhou, Y. Liu, S. Li, Z. Guo, *Nano Lett.* **2017**, *17*, 429.
[11] Z. Tang, C.-h. Tang, H. Gong, *Adv. Funct. Mater.* **2012**, *22*, 1272.
[12] J. Yan, Z. Fan, W. Sun, G. Ning, T. Wei, Q. Zhang, R. Zhang, L. Zhi, F. Wei, *Adv. Funct. Mater.* **2012**, *22*, 2632.
[13] J. Yang, C. Yu, C. Hu, M. Wang, S. Li, H. Huang, K. Bustillo, X. Han, C. Zhao, W. Guo, Z. Zeng, H. Zheng, J. Qiu, *Adv. Funct. Mater.* **2018**, *28*, 1803272.
[14] J. Gong, J.-C. Li, J. Yang, S. Zhao, Z. Yang, K. Zhang, J. Bao, H. Pang, M. Han, *ACS Appl. Mater. Interfaces* **2018**, *10*, 38341.
[15] B. Zhao, L. Zhang, Q. Zhang, D. Chen, Y. Cheng, X. Deng, Y. Chen, R. Murphy, X. Xiong, B. Song, C.-P. Wong, M.-S. Wang, M. Liu, *Adv. Energy Mater.* **2018**, *8*, 1702247.
[16] P. Nakhanivej, X. Yu, S. K. Park, S. Kim, J.-Y. Hong, H. J. Kim, W. Lee, J. Y. Hwang, J. E. Yang, C. Wolverton, J. Kong, M. Chhowalla, H. S. Park, *Nat. Mater.* **2019**, *18*, 156.
[17] S. Bi, H. Banda, M. Chen, L. Niu, M. Chen, T. Wu, J. Wang, R. Wang, J. Feng, T. Chen, M. Dincă, A. A. Kornyshev, G. Feng, *Nat. Mater.* **2020**, *19*, 552.
[18] C. Cheng, G. Jiang, G. P. Simon, J. Z. Liu, D. Li, *Nat. Nanotech.* **2018**, *13*, 685.
[19] J. Xiao, H. Zhan, X. Wang, Z.-Q. Xu, Z. Xiong, K. Zhang, G. P. Simon, J. Z. Liu, D. Li, *Nat. Nanotech.* **2020**, *15*, 683.
[20] Y. Mao, X. Wang, S. Xia, K. Zhang, C. Wei, S. Bak, Z. Shadike, X. Liu, Y. Yang, R. Xu, P. Pianetta, S. Ermon, E. Stavitski, K. Zhao, Z. Xu, F. Lin, X.-Q. Yang, E. Hu, Y. Liu, *Adv. Funct. Mater.* **2019**, *29*, 1900247.
[21] C. Yang, Z. Suo, *Nat. Rev. Mater.* **2018**, *3*, 125.
[22] H. Wang, H. S. Casalongue, Y. Liang, H. Dai, *J. Am. Chem. Soc.* **2010**, *132*, 7472.
[23] S. Li, Y. Zhang, N. Liu, C. Yu, S.-J. Lee, S. Zhou, R. Fu, J. Yang, W. Guo, H. Huang, J.-S. Lee, C. Wang, T. R. Kim, D. Nordlund, P. Pianetta, X. Du, J. Zhao, Y. Liu, J. Qiu, *Joule* **2020**, *4*, 673.
[24] E. Fabbri, M. Nachtegaal, T. Binninger, X. Cheng, B.-J. Kim, J. Durst, F. Bozza, T. Graule, R. Schäublin, L. Wiles, M. Pertoso, N. Danilovic, K. E. Ayers, T. J. Schmidt, *Nat. Mater.* **2017**, *16*, 925.

[25] J. Huang, Q. Shang, Y. Huang, F. Tang, Q. Zhang, Q. Liu, S. Jiang, F. Hu, W. Liu, Y. Luo, T. Yao, Y. Jiang, Z. Pan, Z. Sun, S. Wei, *Angew. Chem., Int. Ed.* **2016**, *55*, 2137.
[26] K. Fan, Y. Ji, H. Zou, J. Zhang, B. Zhu, H. Chen, Q. Daniel, Y. Luo, J. Yu, L. Sun, *Angew. Chem., Int. Ed.* **2017**, *56*, 3289.
[27] S. Li, S.-J. Lee, X. Wang, W. Yang, H. Huang, D. S. Swetz, W. B. Doriese, G. C. O'Neil, J. N. Ullom, C. J. Titus, K. D. Irwin, H.-K. Lee, D. Nordlund, P. Pianetta, C. Yu, J. Qiu, X. Yu, X.-Q. Yang, E. Hu, J.-S. Lee, Y. Liu, *J. Am. Chem. Soc.* **2019**, *141*, 12079.
[28] F. Lin, D. Nordlund, Y. Li, M. K. Quan, L. Cheng, T.-C. Weng, Y. Liu, H. L. Xin, M. M. Doeff, *Nat. Energy* **2016**, *1*, 15004.
[29] E. Hu, X. Yu, R. Lin, X. Bi, J. Lu, S. Bak, K.-W. Nam, H. L. Xin, C. Jaye, D. A. Fischer, K. Amine, X.-Q. Yang, *Nat. Energy* **2018**, *3*, 690.
[30] J. Xu, M. Sun, R. Qiao, S. E. Renfrew, L. Ma, T. Wu, S. Hwang, D. Nordlund, D. Su, K. Amine, J. Lu, B. D. McCloskey, W. Yang, W. Tong, *Nat. Commun.* **2018**, *9*, 947.
[31] H. Fei, J. Dong, M. J. Arellano-Jiménez, G. Ye, N. D. Kim, E. L. G. Samuel, Z. Peng, Z. Zhu, F. Qin, J. Bao, M. J. Yacaman, P. M. Ajayan, D. Chen, J. M. Tour, *Nat. Commun.* **2015**, *6*, 8668.
[32] Y. Zhu, W. Sun, W. Chen, T. Cao, Y. Xiong, J. Luo, J. Dong, L. Zheng, J. Zhang, X. Wang, C. Chen, Q. Peng, D. Wang, Y. Li, *Adv. Funct. Mater.* **2018**, *28*, 1802167.
[33] K. Zhou, W. Zhou, L. Yang, J. Lu, S. Cheng, W. Mai, Z. Tang, L. Li, S. Chen, *Adv. Funct. Mater.* **2015**, *25*, 7530.
[34] Q. Liu, C. Chen, J. Zheng, L. Wang, Z. Yang, W. Yang, *J. Mater. Chem. A* **2017**, *5*, 1421.
[35] K. Zhao, M. Pharr, J. J. Vlassak, Z. Suo, *J. Appl. Phys.* **2010**, *108*, 073517.
[36] B. Ravel, M. Newville, *J. Synchrotron Rad.* **2005**, *12*, 537.
[37] S.-J. Lee, C. J. Titus, R. A. Mori, M. L. Baker, D. A. Bennett, H.-M. Cho, W. B. Doriese, J. W. Fowler, K. J. Gaffney, A. Gallo, J. D. Gard, G. C. Hilton, H. Jang, Y. I. Joe, C. J. Kenney, J. Knight, T. Kroll, J.-S. Lee, D. Li, D. Lu, R. Marks, M. P. Minitti, K. M. Morgan, H. Ogasawara, G. C. O'Neil, C. D. Reintsema, D. R. Schmidt, D. Sokaras, J. N. Ullom, T.-C. Weng, *Rev. Sci. Instrum.* **2019**, *90*, 113101.
[38] M. de Jong, W. Chen, T. Angsten, A. Jain, R. Notestine, A. Gamst, M. Sluiter, C. Krishna Ande, S. van der Zwaag, J. J. Plata, C. Toher, S. Curtarolo, G. Ceder, K. A. Persson, M. Asta, *Sci. Data* **2015**, *2*, 150009.
[39] J. R. Rice, *J. Appl. Mech.* **1968**, *36*, 379.